Bioscience Reports (2025) **00** 1–12
https://doi.org/10.1042/BSR20241173

Research Article

Structural analysis of genetic variants of the human tumor suppressor PALB2 coiled-coil domain

Pothula Purushotham Reddy*, Apurva Phale* and Ranabir Das

National Centre for Biological Sciences, Tata Institute of Fundamental Research, Bangalore, India

Correspondence: Ranabir Das (rana@ncbs.res.in)

The tumor suppressor PALB2 is a key player in the homologous recombination (HR) pathway, functionally connecting BRCA proteins at the DNA damage site. PALB2 forms homodimers via its coiled-coil domain, and during HR, it forms a heterodimeric complex with BRCA1 using the same domain. However, the structural details of the human PALB2 coiled-coil domain are unknown. Several missense variants have been reported in the coiled-coil domain. The structure–function relationship of these variants is poorly understood, posing a challenge to genetic counseling. In this study, we present the solution structure of the human PALB2 coiled-coil domain, which forms an antiparallel homodimer. We then use this structure to investigate the impact of a few well-characterized missense mutations on the fold and interactions of the PALB2 coiled-coil domain. Our findings reveal a strong correlation between the structural impact of mutations and their efficiency in homologous recombination, suggesting that our approach can be applied to study other genetic variations in PALB2. These findings hold promise for improving genetic counseling and advancing cancer research.

Introduction

Double-strand DNA breaks (DSBs) are severe lesions that introduce discontinuity in chromatin. The two major DSB repair pathways are non-homologous end joining (NHEJ) and homologous recombination (HR) [1]. NHEJ is an error-prone mechanism by which DNA ends are joined, whereas HR is a high-fidelity mechanism that uses the sister chromatid as a homologous DNA template for repair. HR starts by creating single-stranded 3′ overhangs through DNA end resection to repair a DNA break. These overhangs are then coated with the ssDNA-binding protein RPA (replication protein A) [1] to safeguard them from degradation and to prevent the formation of non-specific secondary structures. The two breast cancer genes BRCA1 and BRCA2 are crucial in the DNA repair process [2]. The BRCA2–RAD51 protein complex and BRCA1 are recruited to the RPA-coated ssDNA [3]. The BRCA2 protein assists in creating a nucleoprotein filament by loading RAD51 onto the ssDNA, which enables efficient repair of the DNA break. Mutations in BRCA1 and BRCA2 are associated with breast and ovarian cancer susceptibility [4]. *PALB2* (partner and localizer of BRCA2) is another crucial gene associated with susceptibility to breast cancer, Fanconi anemia, and other cancers [5].

The *PALB2* gene encodes an 1186-amino-acid-long protein including the N-terminal coiled-coil domain, ChaM (chromatin association motif) domain, and C-terminal WD40 domain. PALB2 is an essential bridging molecule between BRCA1 and BRCA2 and an integral component of the BRCA complex. The ChaM domain located in the center of the protein is responsible for localizing PALB2 to the chromatin. The C-terminal ring-like B-propeller structure of the WD40 domain of PALB2 interacts with BRCA2 [6]. The WD40 domain also interacts with other essential proteins for HR, such as RAD51, RAD51C, and RNF168 [7,8]. Human PALB2 exists either as a homodimer or as a heterodimer with BRCA1 [9]. The N-terminal coiled-coil domain homodimerizes, and the same domain interacts with BRCA1 to form a heterodimer during HR [10]. Overexpression of the PALB2 coiled-coil domain reduces RAD51 foci formation during HR, indicating a competition between PALB2 homo- and heterodimers [9]. The structure of the mouse PALB2 coiled-coil domain suggests that it forms an antiparallel dimer [11]. However, the structure of the human PALB2 coiled-coil domain is unknown, and the atomistic interactions that regulate the switch from homodimer to heterodimer are poorly understood.

*These authors contributed equally to this work.

Received: 6 September 2024
Revised: 18 December 2024
Accepted: 19 December 2024

Version of Record Published: 14 March 2025

Bioscience Reports (2025) **00** 1–12
https://doi.org/10.1042/BSR20241173

Similar to BRCA1 and BRCA2, PALB2 is a tumor suppressor. A biallelic mutation in PALB2 can cause Fanconi anemia, and monoallelic mutations can increase susceptibility to breast cancer, ovarian cancer, and pancreatic cancer [5]. Multiple variants of uncertain significance (VUS) are present in PALB2 [12]. Most VUS exist within the N-terminal coiled-coil or the C-terminal WD-40 domain (Figure 1A). HeLa cells expressing various VUS were tested for their PARPi (olaparib) sensitivity. L35P, K18R, R37H, and Y28C showed varying degrees of sensitivity. L35P showed the highest sensitivity, with a survival rate below 20%, suggesting severely impaired HR [13]. Functional analysis of a few missense mutations in the PALB2 coiled-coil domain showed varying effects on HR [13–15]. L35P impairs HR by more than 90%. Y28C, R37H, and L24S mutations impair HR by >60% (Figure 1B). It is unclear how these mutations affect the PALB2 homodimer and its switch to heterodimer. The ability to effectively analyze missense mutations in the PALB2 coiled-coil domain and predict the resulting impact on PALB2 function is crucial in evaluating other VUS necessary for genetic counseling.

Here, we have studied the N-terminal coiled-coil domain of human PALB2 (PALB2cc). Biophysical studies confirmed that PALB2cc has a helical secondary structure, forming a homodimer. We then determined the solution structure of PALB2cc, which reveals an antiparallel homodimer. The dimer interface consists of multiple hydrophobic contacts spanning the length of the helix and an aromatic–aromatic interaction at the center. Molecular dynamics simulations suggested that each monomer is unstable due to the exposed hydrophobic residues, and the dimer structure buries them to stabilize the protein. We investigated the impact of specific genetic variants on PALB2cc homodimer and PALB2cc/BRCA1cc heterodimer structures. Our detailed structural analysis demonstrates how these variants modulate the stability of PALB2cc and how this destabilization correlates with PALB2's HR efficiency. This study provides a framework for analyzing other VUS within the PALB2cc domain and predicting their impact on PALB2's activity during DNA repair.

Results

PALB2 coiled-coil domain forms a homodimer

PALB2cc (residue 6-42) was expressed in *Escherichia coli* and purified to evaluate the secondary structure. The secondary structure calculated by circular dichroism (CD) spectroscopy revealed a highly helical (88%) segment (Figure 1C), which is consistent with the predicted coiled-coil domain. PALB2 was studied using analytical size exclusion chromatography to study the oligomerization properties. The protein eluted as a single peak corresponding to the dimer size of 8.9 kDa (Figure 1D).

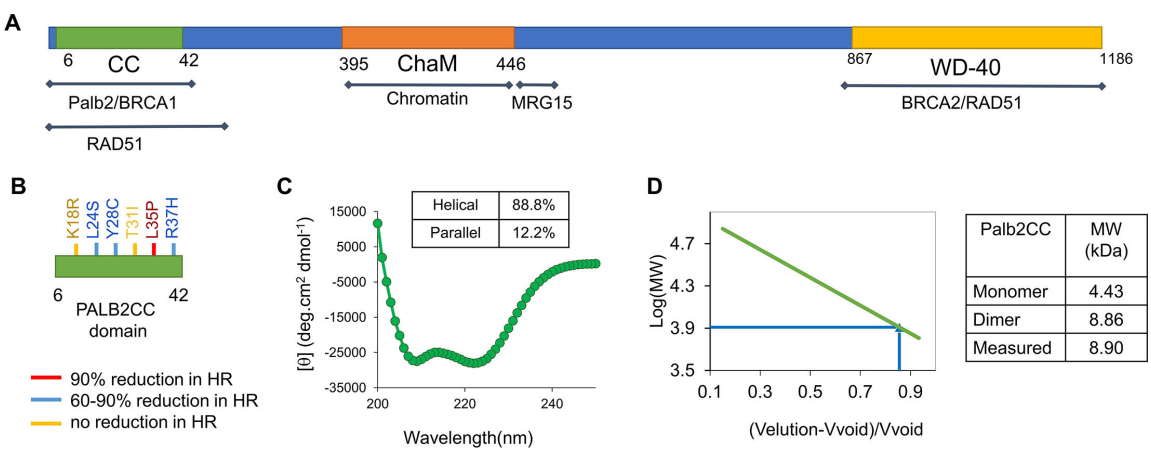

Figure 1: Analysis of the PALB2 coiled-coil domain (PALB2cc) by biophysical techniques.

(A) Schematic representation of the PALB2 protein and its structural domains, along with the known binding sites of its interactors. The coiled-coil domain spans amino acids 6-42. **(B)** A few of the identified variants of the PALB2 in the coiled-coil domain were followed up in this study. The HR values are provided in a previous study by Boonen et al. [13]. **(C)** The CD spectrum of the PALB2cc domain. The helical and parallel β-sheet propensities obtained from fitting the CD data are mentioned at the top. **(D)** The size of the PALB2cc domain is determined by analytical size exclusion chromatography. The plot of molecular weight standards against the elution volume is on the left. Expected monomer, dimer molecular weights, and the measured molecular weight are given on the right.

Structure of the PALB2 coiled-coil domain

The structure of the human PALB2 coiled-coil homodimer was determined using a uniformly labeled ^{13}C, ^{15}N sample. A 0.5 mM lyophilized sample was dissolved in 50 mM Na_2HPO_4, 150 mM NaCl, 5 mM DTT, and pH 6.5 buffer and supplemented with 10% D_2O. All NMR experiments were collected at 25°C using Bruker ASCEND III 600 and 800 MHz NMR spectrometers. Conventional triple resonance experiments were performed to determine the backbone and side chain assignments (Figure 2A). Dihedral angles were calculated using the backbone assignments. The distance constraints were generated from ^{15}N-NOESY-HSQC and ^{13}C-NOESY-HSQC experiments with a mixing time of 100 ms. ^{13}C-filtered NOESY experiments were used to determine the PALB2cc dimer interface. The distance constraints from all NOE experiments and the backbone dihedral angles were used to calculate the solution PALB2cc homodimer structure. The NMR and refinement statistics are provided in Table 1. The structure was further equilibrated in a water box before analysis.

The structure of PALB2cc showed that the domain forms an antiparallel coiled-coil dimer, where the helix in each monomer stretches from residue 11 to 39 (Figure 2B). The buried surface area was 6020 Å^2, suggesting an extensive and stable interface. A robust hydrophobic interaction network holds together the coiled-coil dimer and resembles a leucine zipper structure. The side chains of hydrophobic residues (L9, L17, L21, L24, Y28, T31, and L35) interact across the dimer interface (Figure 2C). At the center of the helices, L24 and Y28 form multiple interactions. Toward the terminal ends, R34 interacts with both K16 and K20. In addition, T31 forms contacts with L17 and L21. L35 packs against L9, L17, and L21. The human PALB2cc domain has 87% sequence identity to the mouse PALB2cc domain (Supplementary figure 1), and their secondary structure and melting points are similar [11]. The tertiary structure of the human PALB2cc domain is also similar overall to the antiparallel orientation of the mouse PALB2cc domain (PDB:6e4h) [11], and several inter-protomer contacts are conserved between the two structures (Supplementary figure 1). However, numerous unique contacts exist between the two structures (Supplementary figure 1). The mouse PALB2 has 64 inter-protomer contacts, while the human PALB2

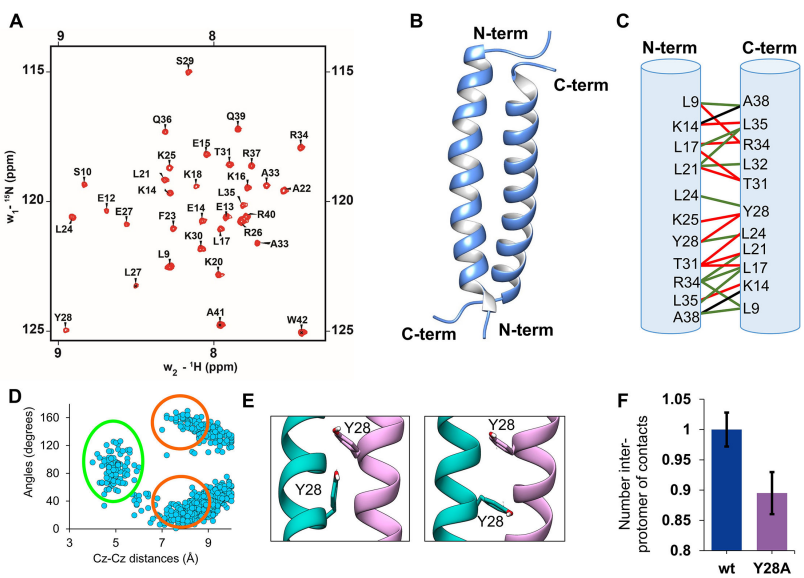

Figure 2: The structure of the PALB2cc domain was studied by NMR spectroscopy and MD simulations.

(A) The ^1H–^{15}N HSQC spectrum of PALB2cc domain (residues:6-41). The assigned backbone N–H amide resonances are labeled. The amide peaks of the first two N-terminal residues (residue numbers 6 and 7) are broadened due to exchange, signifying a dynamic region. Residue number 8 is a proline whose amide peak is not visible in the HSQC. **(B)** The solution structure for the PALB2cc domain suggests an antiparallel orientation between the two helices. **(C)** The contacts between protomers in the PALB2cc dimer are highlighted. Green, black, and red lines connect the interacting residues. The green lines denote hydrophobic contacts. Black lines show the hydrogen bonds, and the red line shows the van der Waals interactions. **(D)** The angle between the aromatic rings of Y28 from each protomer is plotted against the distance between C_z and C_z atom pairs. The cluster of structures with edge-to-face orientation is marked in green, and parallel orientation is marked in red. These were obtained from three ($n = 3$) independent 0.5 µs simulations. **(E)** Snapshots from the MD simulations show the edge-to-face and parallel orientation of the aromatic rings of Y28. **(F)** The number of inter-protomer contacts (normalized) in the wt and Y28A variants are plotted ($P = 0.001$, the number of samples is 3). Normalization was performed by calculating the number of contacts observed in wt-PALB2cc. The error bar represents the standard deviation of three ($n = 3$) independent 0.5 µs simulations.

Bioscience Reports (2025) **00** 1–12
https://doi.org/10.1042/BSR20241173

Table 1: NMR and refinement statistics of human PALB2cc

NOE-based distance constraints	
Intra-residue [i = j]	230
Sequential [| i–j | = 1]	166
Medium range [1 < | i–j | < 5]	144
long-range [| i–j | ≥ 5]	0
Inter chain	96
Total	636
Other restraints	
Dihedral angles (Ψ,Φ)	120
CYANA target function (Å^2)	0.64 ± 0.05
Average pairwise rmsd1 (Å)	
All backbone atoms	1.0 ± 0.2
All heavy atoms	1.5 ± 0.2
Deviations from idealized geometry	
Bond angles (°)	1.6
Bond lengths (Å)	0.009
Close contacts	0
Ramachandran statistics	
Most favored regions (%)	98.7%
Additionally, allowed regions (%)	1.3%
Generously allowed regions (%)	0%
Disallowed regions (%)	0%

has 76 contacts. At the terminal ends, mouse PalB2 is stabilized by hydrophobic contacts between L9 and L35/A38. Human PALB2 is additionally stabilized by van der Waals contacts between K14 and L35/A38. At the center of the homodimer, mouse PALB2 is stabilized by the hydrophobic contacts between L24 of each protomer and a salt bridge between K20 and E27. The human PALB2 lacked these contacts and was replaced by contacts between L21 and T31. Additionally, the human PALB2 is stabilized by the π–π interaction between the Y28 aromatic side chains of each protomer.

Contacts at the dimer interface stabilize the PALB2cc protomers

Aromatic ring geometry is known to play an essential role in determining the fold and topology of the protein. Studies on structural analysis of aromatic π–π interactions in several proteins have shown the preference for either edge-to-face or parallel displaced stacking interaction [16]. We noticed an aromatic π–π interaction between the tyrosine residues (Y28) at the center of the homodimer interface. To analyze the tyrosine interactions, the PALB2cc was simulated by molecular dynamics simulations for 1.5 μs (0.5 μs × 3). The simulations of the PALB2cc domain show that the hydroxy benzene ring of Y28 from both units forms parallel orientation and transiently forms edge-to-face orientation (Figure 2D,E). These interactions may strengthen the interaction network to stabilize the dimer. It has been reported that the Y28A mutant compromises PALB2 function in HR repair and produces hypersensitivity to mitomycin C treatment [17]. We then simulated a variant of Y28A-PALB2cc, which showed a reduction in the inter-protomer contacts (Figure 2F). There was a drop in the intra-helix contacts (Supplementary figure 2), suggesting that the Y28 π–π interaction could significantly stabilize the protomer.

To study the stability of PALB2cc dimers and monomers, a total of 1.5 μs (0.5 μs × 3) MD simulations were run for PALB2cc dimers and monomers using the Amberff03 force field. The helicity of the PALB2cc was maintained throughout the simulation in the dimer. The leucine-rich dimer interface, along with Y28 and T31, maintains the structural integrity of the dimer. In the central region of the helix, L24 from both the monomer units pack against each other. Flanking the central region, the leucine residues L17 and L21 interact with L35 and L32. They create a hydrophobic pocket that is excluded from the solvent.

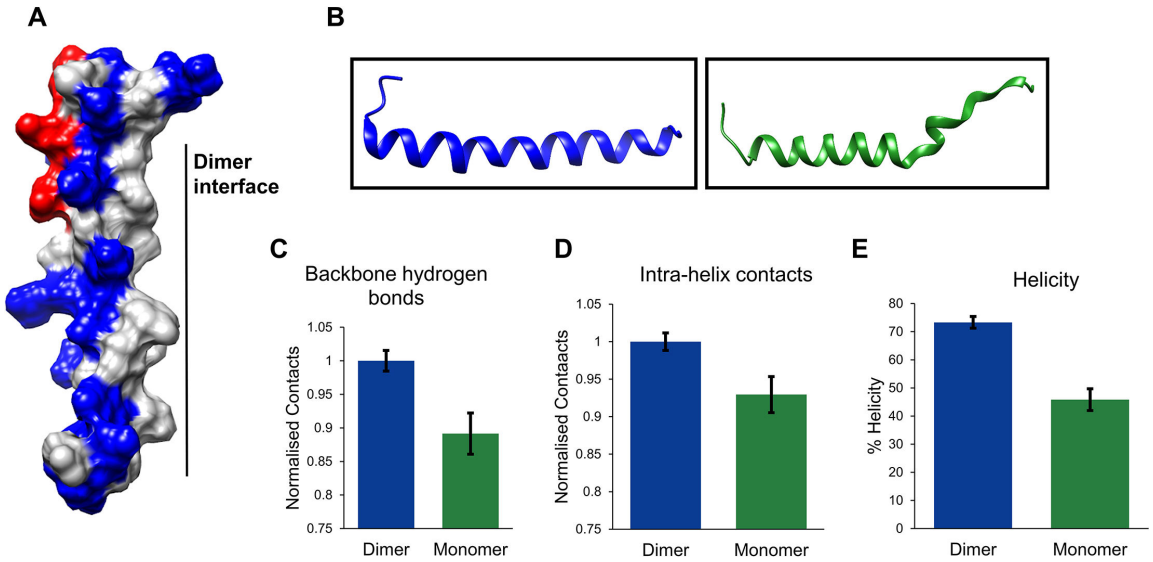

Figure 3: The surface charge distribution and stability of the PALB2cc domain.

(A) Charge distribution on the surface representation of PALB2cc monomer (red—negatively charged, blue—positively charged, and grey—uncharged). **(B)** Snapshots of a single helix from PALB2cc dimer simulation (blue) and monomer simulation (green). The snapshot of **(C)** the number of backbone hydrogen bonds in the PALB2cc dimer and monomer. **(D)** Intra-protomer contacts are plotted for the dimer and monomer. The contacts are measured between all non-hydrogen atoms with a distance cutoff of 7 Å. **(E)** Percentage helicity.

One side of the PALB2cc domain helix is leucine-rich and hydrophobic, essential for dimerization (Figure 3A). The other side of the helix is hydrophilic and has multiple charged amino acids. Due to the numerous lysine and arginine residues on the hydrophilic side, the coiled-coil domain carries a net positive charge. There is an uneven charge distribution along the N-C axis of the helix. The C-terminus is positively charged, as shown in Figure 3A, while the N-terminus has an equal distribution of positively and negatively charged residues. The Cα root mean square fluctuations (RMSF) describe the residue-wise fluctuations observed during the simulations. The Cα RMSF values were higher in the individual monomer than in the dimer (Supplementary figure 3A). When an individual monomer of the PALB2cc was simulated, the monomer unfolded within 0.1 μs (Figure 3B and Supplementary figure 3B and Supplementary figure 3C). This contrasts sharply with the dimer, which was stable for the entire time. The backbone hydrogen bonds, the total intra-protomer contacts, and the helicity were also reduced in the monomer than the dimer (Figure 3C–E), suggesting that the packing of hydrophobic contacts at the dimer interface is essential to maintaining the structural integrity of each unit. Each monomer unit is prone to disorder without the interaction energy from the interfacial contacts.

L35P mutation destabilizes the PALB2cc helix

L35P is a VUS in *PALB2* that may be associated with an increased risk of breast cancer. Functional assays using mouse embryonic stem cells from *PALB2* knockout mice suggested that L35P mutation reduces HR function by more than 90% [18]. It is unclear how the mutation destabilizes PALB2 dimerization and inhibits its interaction with BRCA1. To understand the structural implications of the L35P mutation on the PALB2cc domain, the secondary structure was determined by CD spectroscopy. The helicity in L35P-PALB2cc (25% helical) was reduced compared with wild-type (wt) (88% helical) (Figure 4A). When the molecular weights were determined by analytical size exclusion chromatography, the average molecular mass was reduced from 8.9 kDa for wt-PALB2cc to 6.8 kDa for L35P-PALB2cc (Supplementary figure 4A). The reduced molecular weight implies that the L35P substitution reduces the affinity of the PALB2cc dimer, and the protein population is now a mixture of dimers and monomers.

The stability of the wt-PALB2cc and L35P-PALB2cc was probed by thermal denaturation melt. The thermal stability melting point (T_m) of wt-PALB2cc was 63.4°C. L35P-PALB2cc started unfolding at lower temperatures, suggesting a higher propensity to form disordered structures (Figure 4B). The melting profile of L35P-PALB2cc had a non-cooperative signature, suggesting partially unfolded intermediate states that are in equilibrium with the native and unfolded states. A two-dimensional (2D) $^{1}H–^{15}N$ HSQC for the

Bioscience Reports (2025) **00** 1–12
https://doi.org/10.1042/BSR20241173

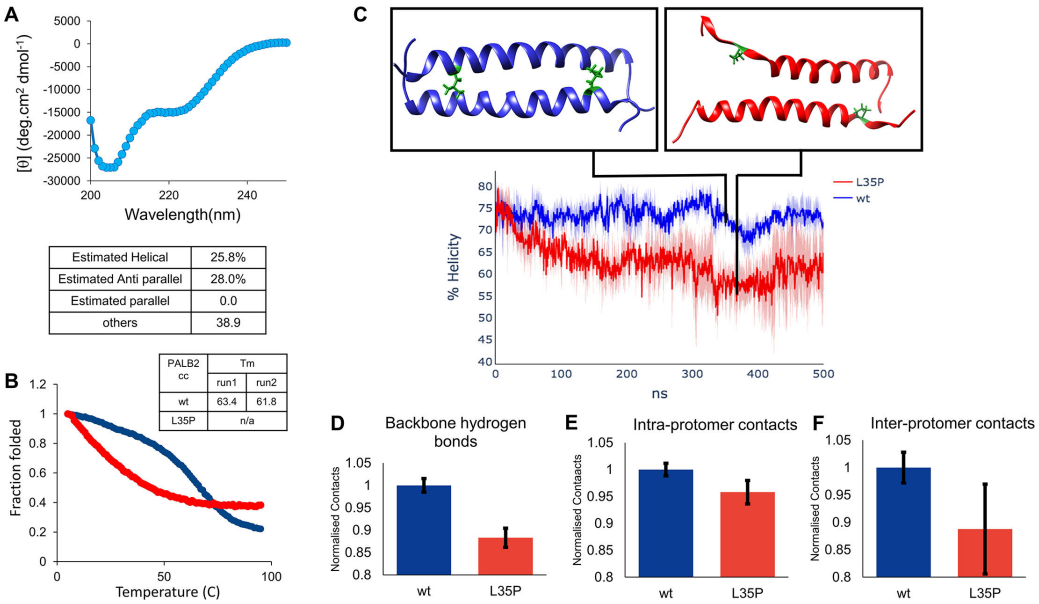

Figure 4: The structural and thermodynamic stability of the L35P-PALB2cc domain was studied by biophysical techniques and MD simulations.

(A) The CD spectrum of the L35P-PALB2cc domain. The % helicity is provided below. **(B)** A representative thermal melt of wt-PALB2cc and L35P-PALB2cc. The melts were performed twice, and the values obtained are provided in a table within the inset. **(C)** From MD simulations, snapshots of the wt-PALB2cc dimer (blue) and L35P-PALB2cc (green). **(D)** The number of backbone hydrogen bonds in wt-PALB2cc and L35P-PALB2cc observed in MD simulations is plotted ($P < 0.01$, the number of samples is 3). **(E)** The number of intra-protomer contacts between all non-hydrogen atoms within the distance of 7 Å in MD simulations is plotted for wt-PALB2cc and L35P-PALB2cc ($P = 0.03$; the number of samples is 3). **(F)** The number of inter-protomer contacts detected between all non-hydrogen atoms in MD simulations is plotted for wt-PALB2cc and L35P-PALB2cc ($P = 0.05$; the number of samples is 3). The y-axis in **(D)**, **(E)**, and **(F)** is normalized by the number of contacts in the wt-PALB2cc. The error bars in **(D)**, **(E)**, and **(F)** represent the standard deviation of three ($n = 3$) independent 0.5 µs simulations.

L35P-PALB2cc mutant was recorded and overlaid with the wt-PALB2cc domain. The backbone amide proton (^{1}H) resonance chemical shift for L35P-PALB2cc spanned a narrower range than the wt-PALB2cc domain, indicating a disordered protein (Supplementary figure 4B).

To further probe the consequence of the L35P mutation on the PALB2cc structure, 1.5 µs MD simulations were performed for the L35P mutation. The C-terminus of the PALB2cc unfolded during the simulation (Figure 4C). Residues around the site of the L35P mutation showed a more significant change in Cα RMSF than wt-PALB2cc, indicating the destabilizing effect of the mutation on the helix (Supplementary figure 4C). The percentage helicity (α-helix) of wt and L35P mutant was calculated using the DSSP tool in Gromacs. The helicity of wt-PALB2 was 74% during simulation, but the L35P mutation decreased the helicity to 62% within 200 ns (Figure 4C). The loss of backbone hydrogen bonds and intra-protomer bonds suggest the partial loss of secondary structure (Figure 4D and E), commensurate with the CD spectroscopy data. Concomitantly, the interprotomer contacts were reduced in the mutant (Figure 4F), reflecting the reduced affinity between dimers observed in the analytical size exclusion chromatography (ASEC) experiment.

Relevance of genetic variants to the structure of PALB2cc homodimer

The variants L24S, R37H, and Y28C in PALB2cc reduce HR by >60%. In contrast, K18R and T31I do not significantly affect HR [13,15]. We simulated all five mutants independently to understand the effect of each mutation on the PALB2cc homodimer. L24 of the two monomers pack against each other at the PALB2cc dimer interface with the Cδ–Cδ distance between the leucine side chain being close to 4 Å. Substitution of L24 to A24 disrupts the dimer interface, and the mutant remains a monomer [11]. Similarly, L24S reduced the inter-protomer contacts in the MD simulations, destabilizing the dimer (Supplementary figures 5 and 6). The contacts of L24 were reduced by 40% when substituted with S24.

R37 did not form substantial intra- or inter-protomer interactions in the wt-PALB2. Substitution of R with H does not significantly affect the charge distribution in the region. In the MD simulations, R37H maintains similar intra- and inter-protomer contacts (Supplementary figure 5) and may not destabilize the PALB2cc dimer. Y28 is at the center of the PALB2cc helix. Since the hydrophobicity of cysteines is high,

the hydrophobicity at the center is maintained in Y28C. However, cysteine has a smaller side chain than tyrosine, and multiple contacts of Y28 are disrupted in the mutant. Moreover, substituting the tyrosine will disrupt the aromatic π–π interaction, destabilizing the homodimer. Overall, the Y28C substantially loses intra- and inter-protomer contacts, which might destabilize the PALB2cc helix (Supplementary figure 6). The substitution K18R does not impact the stability of protomers or the dimer (Supplementary figure 6). The side chain of T31 interacts with the hydrophobic pocket formed by L17, L21, and L24 from the other monomer and L35 from the same chain. Even though this is an interface mutation, the hydrophobicity and side chain geometry are maintained. Consequently, I31 protomer and dimer contacts are conserved (Supplementary figures 5 and 6). The isoleucine replaces the threonine without disrupting the interface, keeping the PALB2cc intact.

PALB2 is phosphorylated at the N-terminus during stress conditions [7]. Ionization radiation induces phosphorylation of PALB2 at serines S59, S157, and S376, which modulates its activity [7]. The coiled-coil domain of PALB2 has two serine residues (S10 and S29) that could be potentially phosphorylated under different stress conditions. S10 is situated at the N-terminal disordered region in PALB2cc, whereas S29 is positioned at the center of the domain. We investigated whether phosphorylation at these serine residues could affect the structure of PALB2. To mimic phosphorylation, we substituted the serine residues with glutamic acid in the domain. The CD spectra and size-exclusion profile of S10E, S29E-PALB2cc, and wt-PALB2cc are similar, suggesting that the secondary structure and size of the domain are unperturbed Supplementary figures 7A and 7B). We also performed MD simulations of PALB2 after replacing the serine side chains with phosphoserines. We found that the intra- and inter-helix contacts in the phosphorylated PALB2 coiled-coil domain were similar to those in the wild-type (Supplementary figures 7C, 7D and 7E), suggesting that phosphorylation may not affect the structure of the coiled-coil domain.

Structural effects of the PALB2 variants on PALB2-BRCA1 heterodimer

We investigated the structural properties of the PALB2 coiled-coil domain in complex with the BRCA1 coiled-coil domain. To achieve this, we created a heterodimeric model using a previously reported structure of the mouse PALB2-BRCA1 (PDB: 7K3S) (Figure 5A). The model was equilibrated for 0.1 μs, and the final structure was used for further simulations for 1.5 μs (0.5 μs × 3). Throughout the entire simulation time, the PALB2–BRCA1 complex remained stable, with both protomers retaining their helicity. The PALB2–BRCA1 heterodimer retains a similar dimer interface as the PALB2 homodimer. The angle between the two helices is 24°. The BRCA1cc domain has a hydrophobic interface that, like the PALB2cc domain, consists of multiple leucine-rich residues. Additionally, the BRCA1cc domain has four positively charged residues and seven negatively charged residues, creating an overall net negative charge. In particular, the C-terminal end of the helix is highly negatively charged. The positively charged N-terminal region of the PALB2cc domain allows for good charge complementarity in the heterodimer interface (Supplementary figure 8).

The hydrophobic residues of PALB2 pack against the hydrophobic face on the BRCA1 coiled-coil domain. The residues L9, L17, L21, L24, Y28, T31, L32, and L35 of the PALB2cc domain engage in multiple contacts with L1392, M1400, L1404, L1407, M1411, L1414, and L1418 residues of BRCA1. Multiple leucine residues on the BRCA1 interface allow for a similar intricate hydrophobic network as observed in the PALB2 homodimer (Supplementary figure 9A). The Y28 aromatic ring of PALB2 is close to M1411 of BRCA1, forming strong met–aromatic interactions between the two protomers [19]. On the other side of Y28, L1404 from the BRCA1 contacts the aromatic ring, forming CH–π interactions (Supplementary figure 9B). In addition to the leucine zipper between the protomers, both these interactions could enhance the stability and strengthen the heterodimeric complex.

To gain further structural insights into the effects of PALB2 variants on the PALB2–BRCA1 interactions, we performed similar simulations as described above. L35P reduces helicity and interprotomer contacts in the PALB2 homodimer. About 50% loss in interfacial contacts is observed in the L35P PALB2–BRCA1 heterodimer (Figure 5B). A reduction in native interfacial contacts was also observed at the mutation site for the L24S and Y28C PALB2 variants. L24 is at the center of the helix, forming multiple interactions with leucine residues of BRCA1. A swap with a polar residue like serine disrupts the native contacts with the BRCA1 up to 30%. Y28C reduces the size of the amino acid, causing loss of met–aromatic and CH–π interaction of the Y28 aromatic ring (Supplementary figures 9C and 9D), overall disrupting the native contacts network below 50%, as seen in Figure 5B.

T31I, R37H, and K18R mutants showed a slight increase in contacts at the mutation site. This is either due to increased side chain size (K18R) or a change in the geometry or polarity (R37H and T31I). The

Bioscience Reports (2025) **00** 1–12
https://doi.org/10.1042/BSR20241173

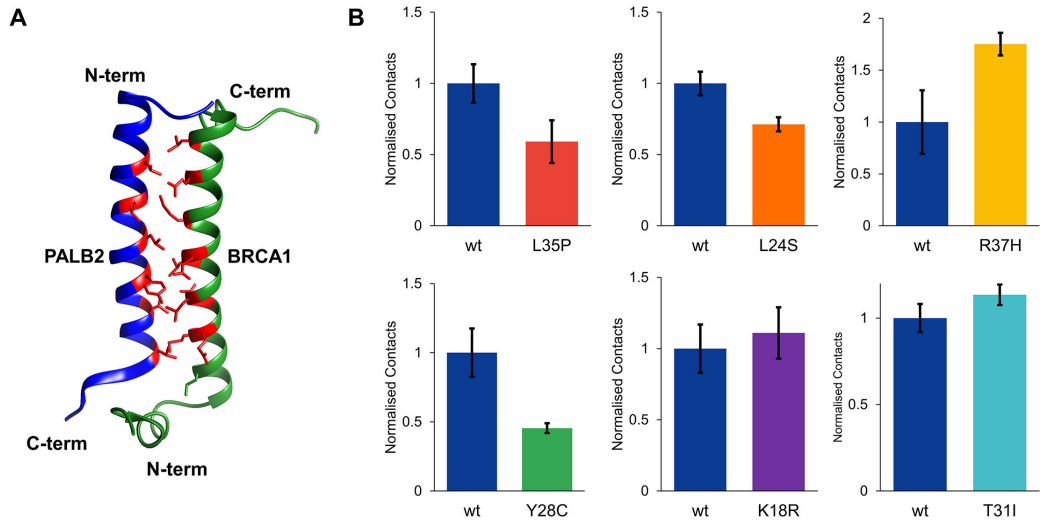

Figure 5: The PALB2-BRCA1 coiled-coil heterodimer was studied using MD simulations.

(A) Modeled with Swiss model after 100 ns simulations (blue—PALB2cc, green—BRCA1cc, and red—dimerization interface residues). **(B)** PALB2cc-BRCA1cc contacts at the site of PALB2 mutation (L35P: $P = 0.023$, L24S: $P < 0.001$, R37H: $P = 0.005$, Y28C: $P < 0.001$, K18R: $P = 0.002$, T31I: $P < 0.001$, and the number of samples is 3). Native contacts are calculated between non-hydrogen atoms with a pairwise distance cutoff of 10 Å. The number of contacts is normalized by the contacts observed in the wild-type PALB2. The error bar represents the standard deviation of three ($n = 3$) independent 0.5 µs simulations.

K18R variant establishes a stronger charged interaction with D1419 from BRCA1. A 20% increase of the occupancy of this salt bridge is observed (Supplementary figure 10). R37 has an electrostatic interaction with D1381, S1387, and D1390 in the PALB2/BRCA1 heterodimers. This allows for partial stabilization of the unstructured N-terminus of BRCA1. H37 retains the contacts with D1381 and S1387 but has reduced interaction with the D1390. However, the overall gain in the total interactions observed at R37H exists. Overall, the L35P, L24S, and Y28C mutations substantially reduce PALB2/BRCA1 interaction, while R37H, T31I, and K18R have more contacts in the PALB2/BRCA1 complex.

Discussion

The tumor suppressor PALB2 functions with the BRCA1 and BRCA2 proteins to maintain genomic integrity by homologous recombination. PALB2 forms a homodimer via its coiled-coil domain. It dissociates from the homodimer to form a heterodimer with the BRCA1 coiled-coil domain. To understand the effect of missense mutations in the coiled-coil domain on the PALB2 structure–function relationship, we solved the human PALB2 coiled-coil domain structure. The solution NMR structure of human PALB2cc suggests it forms an antiparallel homodimer. A network of hydrophobic interactions formed by residues L9, L17, L21, L24, Y28, L35, and A38 drives the dimerization of the PALB2cc domain. These residues in the i + 3 or i + 4 position create a hydrophobic patch complemented by the other protomer. The structure of the human PALB2 coiled-coil domain has unique contacts compared to that of the mouse PALB2 structure and should be the primary reference for evaluating the effects of missense mutations in patients. MD simulations indicated that the monomer coiled-coil domain unfolds rapidly compared with the dimer. Our data suggest that PALB2 homodimerization or its heterodimerization with BRCA1 is essential to the structural integrity of this domain.

Aromatic interactions are essential for protein structure and binding to co-factors [16,20]. An analysis of aromatic interactions in protein structures shows that tyrosine is common at protein interfaces, possibly because the hydroxyl group provides stability when exposed to solvent. The aromatic interactions could be π–π or cation–π interactions. Our simulations suggest that π–π interactions are formed between the side chains of tyrosine 28 from the two PALB2cc protomers. The aromatic interactions between the protomers can further strengthen the hydrophobic interactions for dimerization. The reduced inter-protomer contacts and structural stability of the Y28C mutant underline the importance of aromatic interactions.

The L35P (c.104T > C) mutation was identified from a breast cancer family, a loss of function mutation that disrupts PALB2–BRCA1 interaction [18]. Our MD simulations on the PALB2cc structure suggest the mutation completely disrupts the helical structure at the PALB2cc C-terminal end. Incorporating proline

into an α-helix is challenging due to its lack of an amide proton and the ring formed by its backbone and side chain. Moreover, the proline substitution disrupts multiple critical inter-protomer contacts, leading to a destabilized homodimer. However, the homodimer instability does not increase the heterodimer population because the mutation disrupts essential contacts with BRCA1. Overall, the L35P mutation disrupts the PALB2cc protomer structure, abolishing its self-dimerization and interaction with BRCA1.

We analyzed several missense mutations using the human PALB2cc structure and related them with functional data reported in previous studies (Table 2). Our study shows that the Y28C mutation perturbs the monomer structure and disrupts the homo and heterodimer interactions. The L24S mutation maintains the homodimer PALB2cc structure. However, it significantly disrupts BRCA1 interactions. The R37H mutation maintains structural integrity but reduces homologous recombination (HR) and is sensitive to PARP inhibitors. Possibly, R37H perturbs higher-order complex formation with BRCA proteins by allosteric mechanisms. T31I does not impact PALB2cc monomeric or dimeric structure. Moreover, the functional interactions with BRCA1 are maintained in T31I, which correlates with the unaffected HR. K18R is recruited to the site of DSB more efficiently than WT. This could be due to a stronger association with BRCA1. A similar trend is observed in our simulation studies, where the PALB2 homodimer structure is not hampered, but the PALB2/BRCA1 interactions are enhanced. The structural analysis results of PALB2cc variants reveal a high correlation with their efficiency in HR mechanisms.

The clinical classification of most PALB2 missense mutations is unknown. The overlap between functional analysis and *in silico* structural analysis for PALB2 is poor, partly because, except for the WD40 domain, the structure of human PALB2 domains is largely unknown. The structure of the human PALB2 coiled-coil domain will be helpful for *in silico* predictions. Combining population-based data, *in silico* structural analysis, and functional assays may provide a more robust clinical classification for the PALB2 variants of unknown significance.

Conclusion

Structure determination followed by molecular dynamics has suggested the effect of clinical missense mutations on the PALB2 coiled-coil domain's fold and interactions, consistent with the mutant's efficiency in homologous recombination. The structure and approach will help study other variants of unknown significance in the PALB2 coiled-coil domain.

Materials and methods

Protein expression and purification

A chimeric construct of PALB2 coiled-coil domain (residues 6-42) with N-terminal His-tagged GB1 was cloned into the pET3a vector. For CNBr cleavage, a methionine residue was introduced at the N-terminus of the PALB2 coiled-coil domain. This construct was overexpressed in BL21-DE3 cells in LB media for unlabeled protein and in ^{13}C, ^{15}N enriched M9 media for isotope-labeled protein. The cells were grown till OD_{600} reached 0.6 and were induced with 1 mM IPTG for 4 hours. The cells were harvested, re-suspended in 50 mM Na_2HPO_4, 300 mM NaCl, and 20 mM imidazole (pH 8), and lysed by sonication. The lysate was centrifuged, and the supernatant was incubated with pre-equilibrated Ni^{2+}-NTA beads. The beads were washed, and the protein was eluted with 20%, 40%, and 60% elution buffer (50 mM Na_2HPO_4, 300 mM NaCl, and 500 mM imidazole). Further purification was carried out by a gel filtration column (HiLoad 16/600 Superdex75 pg, GE). The pure fractions were pooled, concentrated to 6 mg/mL, and cleaved by CNBr to remove the N-terminal tags. The cleaved protein was separated with reverse phase column chromatography (RPC) using a gradient of up to 60% methanol with 0.1% TFA. The pure fractions containing PALB2cc collected from RPC were concentrated and lyophilized.

Circular dichroism (CD)

PALB2cc, L35P-PALB2cc, and S10E, S29E-PALB2cc peptides were synthesized from Lifetein technologies. The peptides were dissolved in 50 mM Na_2HPO_4, 150 mM NaCl at pH 6.5 and degassed before measurement. CD measurements were performed on a Jasco CD spectrophotometer in a 1 mm path-length quartz cuvette. Each wavelength scan was performed with 1 nm increments and bandwidth from 250 to 200 nm. The thermal melt experiment was collected with a 1°C increment every 2 minutes. All CD data

Bioscience Reports (2025) **00** 1–12
https://doi.org/10.1042/BSR20241173

Table 2: Effects of mutations in the PALB2 coiled-coil domain

Mutations	Stability of PALB2cc protomer	Stability of PALB2cc homodimer	Stability of PALB2cc heterodimer	Functional phenotype
K18R	No effect	No effect	Slightly enhanced	No effect on HR. Localize to DSB better than wt.
L24S	No effect	No effect	Reduced	Reduced HR by 60%–90%. Loss of binding to BRCA1 and DSB
Y28C	Reduced	Reduced	Reduced	Reduced HR by 60%–90%. Loss of binding to BRCA1 and DSB
T31I	No effect	No effect	Slightly enhanced	No effect on HR
R37H	No effect	No effect	Enhanced	Reduced HR by 60%–90%. Loss of binding to BRCA1 and DSB
L35P	Reduced	Reduced	Reduced	Reduced HR by 90%

were averaged for 10 seconds at each measurement, and the buffer signal was subtracted. Reversibility (often between 70% and 96%) was determined by re-measuring the signal at 222 nm and 20°C.

Analytical size exclusion chromatography (ASEC)

The proteins were dissolved in 50 mM Na_2HPO_4, 150 mM NaCl, 5 mM DTT, and at pH 6.5. The molecular mass of each protein was calculated using an ASEC (HiLoad 30/300 Superdex75 pg, GE) column.

NMR data collection and structure calculation

NMR data for resonance assignments and structure determination were collected at 25°C using Bruker AVANCE III 600 and 800 MHz NMR spectrometers equipped with 5 mm cryoprobes. Complete ^{1}H, ^{13}C, and ^{15}N resonance assignments for PALB2cc were determined using conventional triple-resonance (HNCO, CBCACONH, HNCACB, HCCCONH3D3, HCCCONH3D2, and HCCHTOCSY) NMR methods. Standard 3D ^{15}N-NOESY-HSQC and ^{13}C-NOESY-HSQC experiments with a mixing time of 100 ms were used to get NOE restraints. NMR data processing and analysis were done using NMRpipe [21] and NMRfam_Sparky [22]. The dimer interface on PALB2cc was identified using ^{13}C filtered NOESY experiments on a 1:1 sample of ^{13}C, ^{15}N enriched, and unlabeled (natural abundance) protein. The PALB2cc homodimer structure was calculated using CYANA version 2.1 [23] and refined in XPLOR-NIH. The dihedral angle constraints obtained from TALOS+4 were used for structure calculations. In addition, the intrachain and interchain NOE data were included. The backbone dihedral angles and bond lengths of the final converged structures were evaluated by the Molprobity [24] and PSVS [25] suite of programs. The NMR constraints and refinement statistics are provided in Table 1. The structure and data are deposited with PDB id 8YAP and BMRB id 36647.

Molecular dynamics simulation protocol

The NMR structure of PALB2cc was used to carry out unbiased molecular dynamics simulations. All simulations in this study were performed in Gromacs version 5.1.2 [26] using amber03w.ff [27]. Individual mutations on PALB2cc were created by replacing each side chain from the Dunbrack rotamer library in UCSF Chimera version 1.15 [28]. All the acidic and basic residues were modeled in their charged states. The initial structures were solvated using the TIP4P2005 water model. The net charge in the system was neutralized by adding Na^+ and Cl^- ions. The neutralized system was subjected to energy minimization using the steepest descent minimization in a maximum of 50,000 steps until the maximum force on each atom was less than 1000 kJ/mol/nm. The energy-minimized systems were further equilibrated under constant temperature (NVT) for 100 ps and constant temperature and pressure (NPT) for 100 ps. The temperature was maintained at 300K using a V-rescale Berendsen thermostat with a time constant of 0.1 ps. The pressure was held at 1 bar by employing the Parrinello–Rahman barostat with a time constant of 2 ps. The final production runs were carried out under periodic boundary conditions for 500 ns with a 2 fs time step. The van der Waals and short-range electrostatic interactions were calculated using a 1 nm cutoff. The long-range electrostatics were computed using the particle mesh Ewald method. All bond lengths were constrained using the LINCS algorithm. RMSF, RG, and RMSD were calculated using scripts available

in Gromacs. Percentage α-helicity was calculated using the DSSP tool in Gromacs. The trajectories were converted to Amber format using Pamed. Native contacts for each mutant were computed using CPPTRAJ version 4.14.0 [29] (AmberTools V19.11). The data were plotted using Python in-house scripts.

The phosphoserine PALB2 variant was modeled in UCSF Chimera version 1.15 by replacing S10 and S29 with phosphoserines. An in-house modified amber03w.ff forcefield, which included parameters for phosphoserine, was used to carry out the PALB2 homodimer simulations. The PALB2–BRCA1 structure was modeled by the Swiss model using PDB: 7k3s as a template. The model was then simulated for 100 ns, and the final structure was used for further simulations. A similar protocol to the PALB2 homodimer was followed to simulate the PALB2–BRCA1 heterodimer and the variants of PALB2 in complex with BRCA1. Data analysis was performed similarly. The wild-type and mutants of Palb2 were compared to analyze differences in their helicity, inter-helix and intra-helix native contacts, and hydrogen bonds. Statistical significance for all comparisons throughout the study was determined using a one-tailed t-test for two samples assuming equal variance analysis. The mean of each of the three trajectories for both the wild-type and mutants was used to perform these statistical tests.

Data Availability

The structure of the PALB2 coiled-coil domain is deposited in the Protein Data Bank with PDB ID 8YAP. The associated NMR data are deposited in the Biological Magnetic Resonance Bank ID 36647. The molecular dynamics simulation data and analysis will be provided by the corresponding author upon email request. Other data supporting this study are included within the supporting information.

Competing Interests

The authors declare that they have no conflicts of interest with the contents of this article.

Funding

This work was funded by the Ramalingaswamy Fellowship (BT/RLF/Re-entry/39/2013) awarded by the Department of Biotechnology, Ministry of Science and Technology, India (DBT). It was partially supported by the Tata Institute of Fundamental Research, Department of Atomic Energy, Government of India, under project identification no. RTI 4006 and Science and Engineering Research Board (grant number CRG/2021/006032).

CRediT Author Contribution

PPR: Investigation, Formal Analysis, Validation, Writing-review and editing. AP: Investigation, Formal Analysis, Writing-original draft, Writing-review and editing. RD: Conceptualization, Funding acquisition, Supervision, Writing-review and editing.

Acknowledgments

The NMR data were acquired at the NCBS-TIFR NMR Facility, supported by the Department of Atomic Energy, Government of India, under project no. RTI 4006.

Abbreviations

CD, circular dichroism; ChaM, chromatin association motif; DSBs, double-strand DNA breaks; HR, homologous recombination; NHEJ, non-homologous end joining; PALB2, partner and localizer of BRCA2; RMSF, root mean square fluctuations; RPA, replication protein A; RPC, reverse phase column chromatography; VAS, variants of uncertain significance.

References

1 Wright, W.D., Shah, S.S. and Heyer, W.D. (2018) Homologous recombination and the repair of DNA double-strand breaks. *J. Biol. Chem.* **293**, 10524–10535 https://doi.org/10.1074/jbc.TM118.000372
2 Gorodetska, I., Kozeretska, I. and Dubrovska, A. (2019) BRCA genes: the role in genome stability, cancer stemness and therapy resistance. *J. Cancer* **10**, 2109–2127 https://doi.org/10.7150/jca.30410
3 Bell, J.C., Dombrowski, C.C., Plank, J.L., Jensen, R.B. and Kowalczykowski, S.C. (2023) BRCA2 chaperones RAD51 to single molecules of RPA-coated ssDNA. *Proc. Natl. Acad. Sci. U.S.A.* **120**, e2221971120 https://doi.org/10.1073/pnas.2221971120

4 Stoppa-Lyonnet, D. (2016) The biological effects and clinical implications of BRCA mutations: where do we go from here? *Eur. J. Hum. Genet.* **24**, S3–S9 https://doi.org/10.1038/ejhg.2016.93
5 Ducy, M., Sesma-Sanz, L., Guitton-Sert, L., Lashgari, A., Gao, Y., Brahiti, N, et al. (2019) The tumor suppressor PALB2: inside out. *Trends Biochem. Sci.* **44**, 226–240 https://doi.org/10.1016/j.tibs.2018.10.008
6 Oliver, A.W., Swift, S., Lord, C.J., Ashworth, A. and Pearl, L.H. (2009) Structural basis for recruitment of BRCA2 by PALB2. *EMBO Rep.* **10**, 990–996 https://doi.org/10.1038/embor.2009.126
7 Wu, S., Zhou, J., Zhang, K., Chen, H., Luo, M., Lu, Y, et al. (2020) Molecular mechanisms of PALB2 function and its role in breast cancer management. *Front. Oncol.* **10**, 1–13 https://doi.org/10.3389/fonc.2020.00301
8 Park, J.Y., Singh, T.R., Nassar, N., Zhang, F., Freund, M., Hanenberg, H. et al. (2014) Breast cancer-associated missense mutants of the PALB2 WD40 domain, which directly binds RAD51C, RAD51 and BRCA2, disrupt DNA repair. *Oncogene* **33**, 4803–4812 https://doi.org/10.1038/onc.2013.421
9 Buisson, R. and Masson, J.Y. (2012) PALB2 self-interaction controls homologous recombination. *Nucleic Acids Res.* **40**, 10312–10323 https://doi.org/10.1093/nar/gks807
10 Zhang, F., Ma, J., Wu, J., Ye, L., Cai, H., Xia, B. et al. (2009) PALB2 links BRCA1 and BRCA2 in the DNA-damage response. *Curr. Biol.* **19**, 524–529 https://doi.org/10.1016/j.cub.2009.02.018
11 Song, F., Li, M., Liu, G., Swapna, G.V.T., Daigham, N.S., Xia, B. et al. (2018) Antiparallel coiled-coil interactions mediate the homodimerization of the DNA damage-repair protein PALB2. *Biochemistry* **57**, 6581–6591 https://doi.org/10.1021/acs.biochem.8b00789
12 Rodrigue, A., Margaillan, G., Gomes, T.T., Coulombe, Y., Montalban, G.,Carvalho,S.D.C.E.S.et al. (2019) A global functional analysis of missense mutations reveals two major hotspots in the PALB2 tumor suppressor. *Nucleic Acids Res.* **47**, 10662–10677 https://doi.org/10.1093/nar/gkz780
13 Boonen, R.A.C.M., Rodrigue, A., Stoepker, C., Wiegant, W.W., Vroling, B., Sharma, M. et al. (2019) Functional analysis of genetic variants in the high-risk breast cancer susceptibility gene PALB2. *Nat. Commun.* **10**, 5296 https://doi.org/10.1038/s41467-019-13194-2
14 Boonen, R.A.C.M., Vreeswijk, M.P.G.van AttikumH.2020) Front Mol Biosci. *Funct. charact. of PALB2 variants of uncert. signif toward cancer risk and therapy resp. predict.* **7**, 169 https://doi.org/10.3389/fmolb.2020.00169
15 Rodrigue, A., Margaillan, G., Torres Gomes, T., Coulombe, Y., Montalban, G.,Carvalho,S.D.C.E.S.et al. (2019) A global functional analysis of missense mutations reveals two major hotspots in the PALB2 tumor suppressor. *Nucleic Acids Res.* **47**, 10662–10677 https://doi.org/10.1093/nar/gkz780
16 Anjana, R., Vaishnavi, M.K., Sherlin, D., Kumar, S.P., Naveen, K., Kanth, P.S. et al. (2012) Aromatic-aromatic interactions in structures of proteins and protein-DNA complexes: a study based on orientation and distance. *Bioinformation* **8**, 1220–1224 https://doi.org/10.6026/97320630081220
17 Sy, S.M.H., Huen, M.S.Y. and Chen, J. (2009) PALB2 is an integral component of the BRCA complex required for homologous recombination repair. *Proc. Natl. Acad. Sci. U.S.A.* **106**, 7155–7160 https://doi.org/10.1073/pnas.0811159106
18 Foo, T.K., Tischkowitz, M., Simhadri, S., Boshari, T., Zayed, N., Burke, K.A. et al. (2017) Compromised BRCA1-PALB2 interaction is associated with breast cancer risk. *Oncogene* **36**, 4161–4170 https://doi.org/10.1038/onc.2017.46
19 Chatterjee, K.S. and Das, R. (2021) An "up" oriented methionine-aromatic structural motif in SUMO is critical for its stability and activity. *J. Biol. Chem.* **297**, 100970 https://doi.org/10.1016/j.jbc.2021.100970
20 Chatterjee, K.S., Tripathi, V. and Das, R. (2019) A conserved and buried edge-to-face aromatic interaction in small ubiquitin-like modifier (SUMO) has A role in SUMO stability and function. *J. Biol. Chem.* **294**, 6772–6784 https://doi.org/10.1074/jbc.RA118.006642
21 Delaglio, F., Grzesiek, S., Vuister, G.W., Zhu, G., Pfeifer, J. and Bax, A. (1995) NMRPipe: A multidimensional spectral processing system based on UNIX pipes. *J. Biomol. NMR.* **6**, 277–293 https://doi.org/10.1007/BF00197809
22 Lee, W., Tonelli, M. and Markley, J.L. (2015) NMRFAM-SPARKY: enhanced software for biomolecular NMR spectroscopy. *Bioinformatics* **31**, 1325–1327 https://doi.org/10.1093/bioinformatics/btu830
23 Gottstein, D., Kirchner, D.K. and Güntert, P. (2012) Simultaneous single-structure and bundle representation of protein NMR structures in torsion angle space. *J. Biomol. NMR.* **52**, 351–364 https://doi.org/10.1007/s10858-012-9615-8
24 Williams, C.J., Headd, J.J., Moriarty, N.W., Prisant, M.G., Videau, L.L., Deis, L.N. et al. (2018) MolProbity: More and better reference data for improved all-atom structure validation. *Protein Sci.* **27**, 293–315 https://doi.org/10.1002/pro.3330
25 Bhattacharya, A., Tejero, R. and Montelione, G.T. (2007) Evaluating protein structures determined by structural genomics consortia. *Proteins* **66**, 778–795 https://doi.org/10.1002/prot.21165
26 Abraham, M.J., Murtola, T., Schulz, R., Páll, S., Smith, J.C., Hess, B. et al. (2015) GROMACS: High performance molecular simulations through multi-level parallelism from laptops to supercomputers. *SoftwareX* **1–2**, 19–25 https://doi.org/10.1016/j.softx.2015.06.001
27 Duan, Y., Wu, C., Chowdhury, S., Lee, M.C., Xiong, G., Zhang, W. et al. (2003) A point-charge force field for molecular mechanics simulations of proteins based on condensed-phase quantum mechanical calculations. *J. Comput. Chem.* **24**, 1999–2012 https://doi.org/10.1002/jcc.10349
28 Pettersen, E.F., Goddard, T.D., Huang, C.C., Couch, G.S., Greenblatt, D.M., Meng, E.C. et al. (2004) UCSF Chimera--A visualization system for exploratory research and analysis. *J. Comput. Chem.* **25**, 1605–1612 https://doi.org/10.1002/jcc.20084
29 Roe, D.R. and Cheatham, T.E. (2013) PTRAJ and CPPTRAJ: Software for processing and analysis of molecular dynamics trajectory data. *J. Chem. Theory Comput.* **9**, 3084–3095 https://doi.org/10.1021/ct400341p